Ostovari Moghaddam A., Shokuhfar A., Zhang Y., Zhang T., Cadavid D., Arbiol J., Cabot A.. Ge-Doped ZnSb/ß-Zn4Sb3 Nanocomposites with High Thermoelectric Performance. Advanced Materials Interfaces, (2019). 6. 1900467: - . 10.1002/admi.201900467,

Ge-doped ZnSb/β-Zn_4Sb_3 nanocomposites with high thermoelectric performance

Ahmad Ostovari Moghaddam, Ali Shokuhfar, Yu Zhang, Ting Zhang, Doris Cadavid, Jordi Arbiol, Andreu Cabot**

Dr. A. Ostovari Moghaddam, Prof. Ali Shokuhfar
Advanced Materials and Nanotechnology Research Laboratory, Faculty of Materials Science and Engineering, K. N. Toosi University of Technology, Tehran, Iran
E-mail: ostovary@aut.ac.ir

Y. Zhang, Prof. D. Cadavid, Prof. A. Cabot
Catalonia Institute for Energy Research – IREC, 08930 Sant Adrià de Besòs, Spain
E-mail: acabot@irec.cat

T. Zhang, Prof. J. Arbiol
Catalan Institute of Nanoscience and Nanotechnology (ICN2), CSIC and BIST, Campus UAB, Bellaterra, 08193 Barcelona, Spain

Prof. D. Cadavid
Departamento de Física, Universidad Nacional de Colombia, 111321, Ciudad Universitaria, Bogotá, Colombia.

Prof. J. Arbiol and Prof. A. Cabot
ICREA, Pg. Lluis Companys 23, 08010 Barcelona, Spain

Keywords: Nanocomposite, Thermoelectric, β-Zn_4Sb_3, ZnSb, Ball milling

ZnSb/β-Zn_4Sb_3 nanocomposites were produced from $Zn_{1.1-x}Ge_xSb$ (x = 0, 0.01, 0.02, 0.04, 0.06) mixtures using a two-step process. First, proper amounts of the three elements were mixed, melted and reacted at 800 K. During this process, the non-stoichiometric mixture crystallized in a combination of ZnSb and β-Zn_4Sb_3 phases. In a second step, this material was ball milled and subsequently hot pressed. Through this process, a dense ZnSb/β-Zn_4Sb_3 composite, consisting of β-Zn_4Sb_3 nanoinclusions embedded within a ZnSb matrix, was formed. The particular phase distribution of the final ZnSb/β-Zn_4Sb_3 composites was a consequence of the harder and more brittle nature of ZnSb compared to Zn_4Sb_3, which translated into a stronger reduction of the size of the ZnSb crystal domains during ball milling. We hypothesize that this small particle size and the high temperature generated during ball milling, resulted in the melting of the ZnSb phase during the ball milling process and the posterior crystallization of the two phases in a ZnSb/β-Zn_4Sb_3 matrix/nanoinclusion-type phase distribution. This particular phase distribution and the presence of Ge resulted in excellent thermoelectric performances, with power factors up to 1.5 $mWm^{-1}K^{-2}$, lattice thermal conductivities down to 0.74 $Wm^{-1}K^{-1}$ and ZT values up to 1.2 at 650 K, which is among the highest ZT values reported for ZnSb.

1. Introduction

Intermetallic compounds with wide compositional ranges and a broad variety of crystal structures provide exciting platforms for both basic research and technological application. In particular, the Zn-Sb binary system displays several intermetallic phases that show complex defect structures and are characterized by excellent transport properties. Several phases of this system have been proposed for thermoelectric (TE) application as alternatives to materials based on expensive and rare elements such as Bi-Te alloys. These Zn-Sb phases include $Zn_{1+\delta}Sb$,[1, 2] β-Zn_8Sb_7,[3] $Zn_{9-\delta}Sb_7$,[4] α-Zn_3Sb_2,[5] $Zn_{3-x}Sb_2$,[6] ZnSb and β-Zn_4Sb_3. $Zn_{1+\delta}Sb$, which has been synthesized just in nanocrystal form, was predicted to crystallize in a P1 space group consisting of 10 Sb^{4-} dimers, 8 isolated Sb^{3-} anions and 32 Zn^{2+} cations.[1] β-Zn_8Sb_7, a new metastable phase with Zn_8Sb_7 composition, has been synthesized via high temperature solid state reaction followed by quenching. β-Zn_8Sb_7 crystallizes in a non-centrosymmetric orthorhombic space group Pmn21 (No. 31) with unit cell parameters a = 15.029(1) Å, b = 7.7310(5) Å and c = 12.7431(9) Å.[3] Within the $Zn_{9-\delta}Sb_7$ subsystem, an α polymorph and a Zn-poorer β polymorph with the same hexagonal structure (P6/mmm) but different lattice parameters exist in the temperature range from 514 °C to 581 °C. The atomic arrangement in $Zn_{9-\delta}Sb_7$ consists of 3 Sb^{2-} dimers and 4 isolated Sb^{3-} ions with 9 Zn^{2+} cations.[4] α-Zn_3Sb_2 quenches in a big hexagonal cell in space group $R\bar{3}$ (a = 15.212(2), c =

74.83(2) Å), where isolated Sb^{3-} anions construct tetrahedral voids filled with highly disordered Zn^{2+} cations.[5] The chemical composition of $Zn_{3-x}Sb_2$ is $(Zn^{2+})_{17+\alpha}(Sb^{3-})_{10+2\alpha}(Sb^{2-})_{2-2\alpha}$, where α (< 1) is the fraction of unpaired Sb^6 atoms. Generally, the composition can be written as $Zn_{17+\alpha}Sb_{12}$, which is distinct from the Zn_3Sb_2 phase that contains only Sb^{3-} anions.[6] All these phases are stable in just a relatively narrow range of temperatures well above ambient, and in the best case scenario they are metastable at room temperature. This instability inhibits their practical application.[3-5]

β-Zn_4Sb_3 exhibits the highest TE performance within the Zn-Sb system, with a TE figure of merit, *ZT*, up to 1.4 at 748 K.[7] However, its moderate stability is a major unsolved issue. β-Zn_4Sb_3 can decompose to Zn and ZnSb at temperatures below 500 K, what hinders its practical application.[7-9] The high ZT values reached for this material are associated with the complex hexagonal crystal structure of β-Zn_4Sb_3 with space group $R\bar{3}c$, which results in a very low thermal conductivity.[10] The crystal structure of β-Zn_4Sb_3 consists of 6 Sb_2^{4-} dimers and 18 isolated Sb^{3-} anions, which need 39 Zn^{2+} cations to maintain the charge balance. This structure provides β-Zn_4Sb_3 with a glass-like thermal conductivity mainly due to the anharmonic motion of the Sb1 atoms coordinated only by Zn atoms.[11] It is also agreed that both interstitial and disordered Zn sites further reduce the already low thermal conductivity of β-Zn_4Sb_3.[12] Taking advantage of this low thermal conductivity and a significant Seebeck coefficient, several elements has been introduced in small quantities to optimize the charge carrier concentration of this material and to maximize in this way its ZT,[13-15] e.g. Al,[16] Ga,[16] In,[16, 17] Hg,[18] Cd,[19] Nb,[20] Te,[21, 22] Mg,[23] Ag,[12] Cu,[24] Fe,[25] Bi,[26] Se,[27] Pb,[28] and Ge.[29] Numerous studies have been also devoted to study the thermal decomposition of this phase, its major issue, and to improve it through doping with elements such as Pb, Cd and Ag.[12, 19, 28] However, these progresses has not yet meet all the requirements for practical applications, and improving stability remains as a major challenge to be solved for this material.

From a practical point of view, ZnSb not only provides the second highest TE performances within the Zn-Sb system, but it is also the only phase in this system with a proper stability for real TE application. ZnSb crystalizes in an orthorhombic crystal structure (space group Pbca) which contains 8 Zn^{2+} cations and 4 Sb^{24-} dimers per unit cell. ZnSb possesses higher power factors than β-Zn_4Sb_3, but its relatively higher thermal conductivity, related to its simpler crystal structure, leads to overall lower TE performance.[30] A common approach to reduce the thermal conductivity of this material is through grain refinement to nanoscale dimension.[31-33] Okamura *et al.*[34] synthesized ZnSb by the melting approach and used mechanical grinding as a post synthesis treatment to reduce its thermal conductivity. Using this strategy, they reduced the thermal conductivity to 1.41 $Wm^{-1}K^{-1}$ at room temperature and reached a maximum ZT value of 0.8 at 550 K. Thermal conductivities below 1 $Wm^{-1}K^{-1}$ have been also reported for nanostructured ZnSb prepared by cryo-milling and hot pressing.[35] An alternative approach to decrease the thermal conductivity of ZnSb is the incorporation of a second phase in the form of nano-inclusions. This strategy was used in Valset et *al.*[36] work, where a *ZT* value close to unity at 550 K was realized in Cu-doped ZnSb containing 2.5 at% of Zn_3P_2 nanoparticles. The high ZT values reached for this nanocomposite were attributed to a 15% reduction in the thermal conductivity and a modulation doping effect. The same strategy was also used in ZnSb doped with Ag (0.15 at%), Cd (3 at%) and Sn (3 at%), resulting in $ZT = 1$ at 630 K.[37] The highest *ZT* value for ZnSb was reported by Xiong *et al.*[14] in Ag-doped $Zn_{1-x}Ag_xSb$ ($x = 0.002$), which reached $ZT = 1.15$ at 570 K. Being ZnSb the most stable intermetallic phase in the Zn-Sb binary system, to further explore this system through alternative doping elements and phases is a worth endeavor. In this scenario, one potentially interesting dopant that is yet to be systematically investigated is Ge.

In this work, we study the in-situ preparation of ZnSb/β-Zn_4Sb_3 nanocomposites through ball milling off-stoichiometric Zn-Sb mixtures. We additionally analyze the effects of Ge doping on the TE performance of the obtained ZnSb/β-Zn_4Sb_3 composites.

2. Results and discussion

2.1. Phase and structure

Ge-doped ZnSb/β-Zn_3Sb_4 nanocomposites with nominal compositions $Zn_{1.1-x}Ge_xSb$ (x = 0, 0.01, 0.02, 0.04, 0.06) were produced in a two-step process (see details in experimental section). First, proper amounts of the three elements were reacted at high temperature. In a second step, ingots were ground in an agate mortar and placed into a zirconia jar to ball mill them for 20 h using tungsten carbide balls. Ball milled powders were loaded into a 8 mm diameter graphite die and hot pressed under argon atmosphere at 400 ºC for 5 min, under a pressure of 100 MPa. The obtained pellets were finally annealed at 380 ºC for 1 h under Ar atmosphere.

Using this procedure, $Zn_{1.1-x}Ge_xSb$ compounds with relative densities ~95% were obtained. The crystal phase of hot-pressed $Zn_{1.1-x}Ge_xSb$ nanomaterials was resolved by XRD (**Figure 1**). The un-substituted $Zn_{1.1}Sb$ sample was composed of ZnSb and β-Zn_4Sb_3 phases (JCPDS cards 96-900-8883 and 96-400-1475). Rietveld refinement analysis using GSAS-II software (**Figure S1**) allowed determining the phase fractions of the $Zn_{1.1}Sb$ sample to be 59.7 % ZnSb and 40.3 % β-Zn_4Sb_3. No XRD peak corresponding to un-reacted Zn or Sb were observed.

For all Ge-substituted samples, XRD data was also consistent with a mixture of ZnSb and β-Zn_4Sb_3 phases. As the Ge content increased, XRD patterns more clearly resembled that of pure ZnSb phase. At high Ge substitutional levels, the excess of Zn to form β-Zn_4Sb_3 was strongly decreased and just a minor amount of β-Zn_4Sb_3 could be detected in the XRD patterns. Quantitative Rietveld analyses indicated that the amount of β phase decreased from 40.3 % for the un-substituted sample (x = 0) to 14 % for x = 0.06. Besides, a weak peak corresponding to elemental Ge could be already detected in XRD patterns of samples with x = 0.01, and increasingly higher amounts of elemental Ge were observed for substitution levels of x = 0.02 and above.

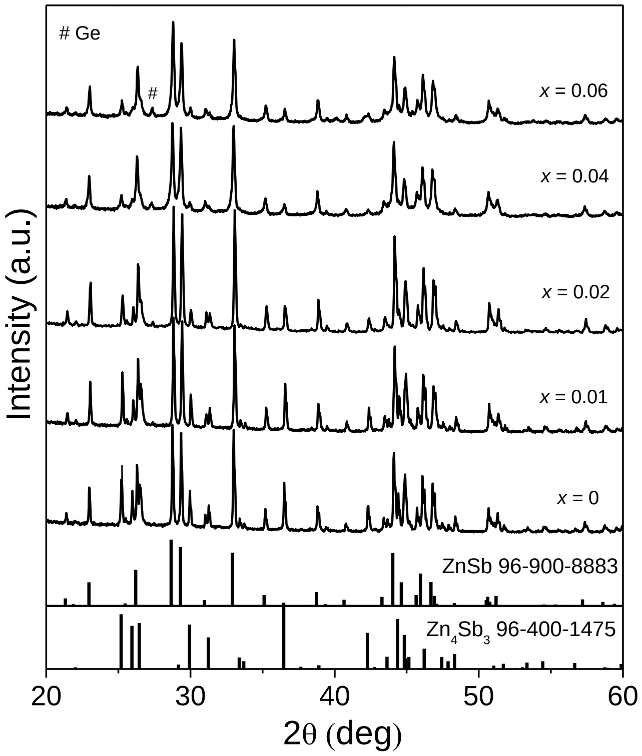

Figure 1. XRD patterns of $Zn_{1.1-x}Ge_xSb$ compounds. Reference patterns for β-Zn_4Sb_3 (JCPDS 96-400-1475) and ZnSb (JCPDS 96-900-8883) are also plotted for comparison.

2.2. Microstructural characterization

After 20 h of ball milling, nanopowders consisted of agglomerated nanoparticles with sizes between 10 and 30 nm. A high tendency to agglomeration was systematically observed and despite long-time sonication during preparation of TEM samples, individual particles were rarely observed during TEM studies. Hot-pressed and annealed pellets after manual grinding for TEM and SEM sample preparation presented irregular shaped particles with different sizes (**Figure S2**). Both, coarse grains and nanodomains with sizes between 50 and 500 nm were observed, indicating clear growth of the agglomerated nanoparticles during hot pressing and posterior annealing. Identical morphological characteristics were observed for all samples, regardless of doping content (Figure S2b and c).

HRTEM characterization of $Zn_{1.09}Ge_{0.01}Sb$ composites showed them to contain different crystallographic domains (Figure 2). Power spectrum analysis of the different regions observed in HRTEM micrographs allowed discerning two different crystal phases. In Figure 2, the power spectrum of region 1 (R1) revealed the selected crystal structure to match with the $Zn_{3.878}Sb_3$ hexagonal phase (space group =R3-CH) with a=b=12.2406 Å and c=12.4361 Å). From this particular HRTEM micrograph, the $Zn_{3.878}Sb_3$ lattice fringe distances were measured to be 0.249 nm, 0.202 nm and 0.299 nm, at 41.99 º and 96.10º, which we interpreted as the $Zn_{3.878}Sb_3$ phase visualized along its [11-20] zone axis. For the rectangular area in region 2 (R2), the lattice fringe distances were measured to be 0.194 nm, 0.209 nm and 0.132 nm, at 50.92 º and 83.59º, which we interpreted as the orthorhombic ZnSb phase (space group =Pbca) with a=6.2016 Å, b=7.7416 Å and c=8.0995 Å, visualized along its [-121] zone axis. The comparison between the experimental and the theoretical bulk plane spacing and angles is detailed in Table S1. Overall, extensive HRTEM analysis indicated that β-Zn_4Sb_3 crystal domains were usually surrounded by the ZnSb phase, with different phase ratios depending on the initial Zn-Sb stoichiometry. HRTEM characterization also demonstrated the poly/nanocrystalline nature of the composite and the high crystallinity of the different domains.

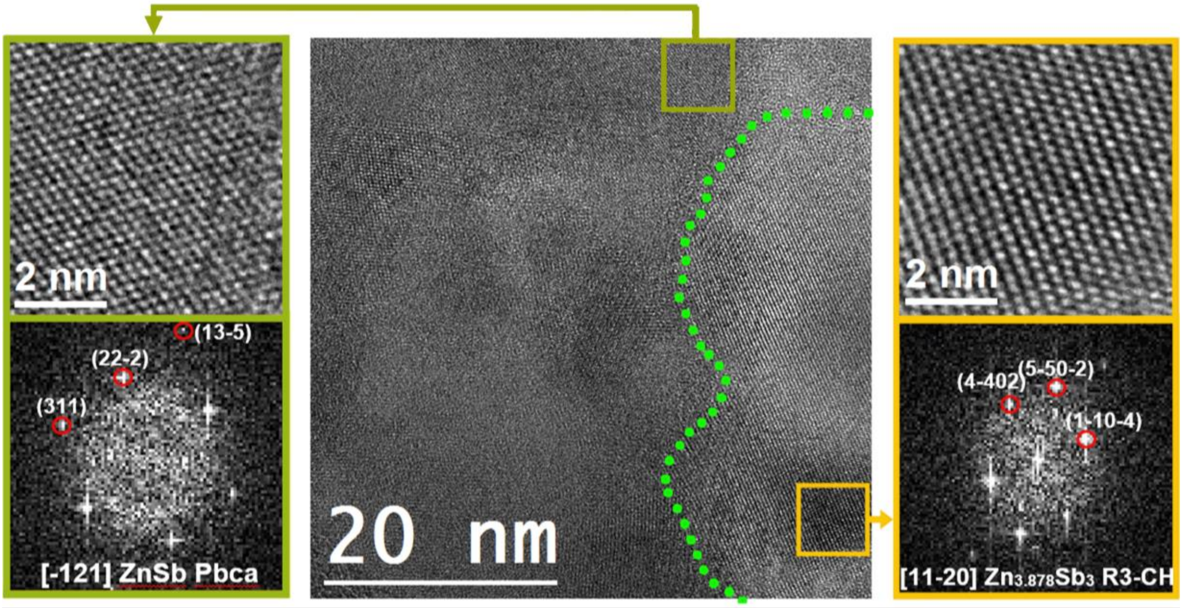

Figure 2. HRTEM micrograph of the consolidated $Zn_{1.09}Ge_{0.01}Sb$ sample showing the interface between different crystallographic phases. The green dotted line limits a β-Zn_4Sb_3 crystal domain. Enlarged images from the rectangular areas and the corresponding power spectrum are also shown.

The compositional distribution within the nanocomposite was further evaluated by HAADF-STEM and EELS chemical composition maps (Figure 3). EELS compositional maps confirmed the presence of the three elements, Zn, Sb and Ge, all through the nanopowder. While Ge was distributed homogeneously through the sample, an slightly uneven distribution of Zn and Sb was observed. Most crystal domains of the $Zn_{1.09}Ge_{0.01}Sb$ sample displayed Sb-rich shells and Zn-rich cores. Taking into account the XRD and HRTEM results displaying the existence of both the ZnSb and β-Zn_4Sb_3 phases within the sample and the absence of elemental Zn and Sb phases, we attribute the Sb-rich shell to the ZnSb phase and the Zn-rich internal core to the β-Zn_4Sb_3 phase.

Considering the above results, we visualize the phase distribution within the nanocomposite as consisting in β-Zn_4Sb_3 grains within a ZnSb matrix. We hypothesize the formation process of such ZnSb/β-Zn_4Sb_3 nanocomposite as schematized in Figure 3b. During the high energy ball-milling process, the pre-synthesized $Zn_{1-x}Ge_xSb$ bulky sample composed of β-Zn_4Sb_3 and ZnSb phases (Figure S3) is shattered by the severe impact of tungsten carbide balls. During ball milling, the ZnSb refines to nanoscale more rapidly than β-Zn_4Sb_3 because of its higher hardness and lower impact toughness.[38-40] ZnSb nanocrystals may partially melt during ball milling and its fluid nature may facilitate the coating of the larger β-Zn_4Sb_3 particles to form β-Zn_4Sb_3@ZnSb core@shell structures. Such core-shell structures were found homogeneously dispersed within the remaining ZnSb matrix forming the ZnSb/β-Zn_4Sb_3 nanocomposite. XRD analysis of pre-synthesized samples confirmed that ball milling acted as a medium for redistribution of the two phases without substantial structural changes (Figure S3).

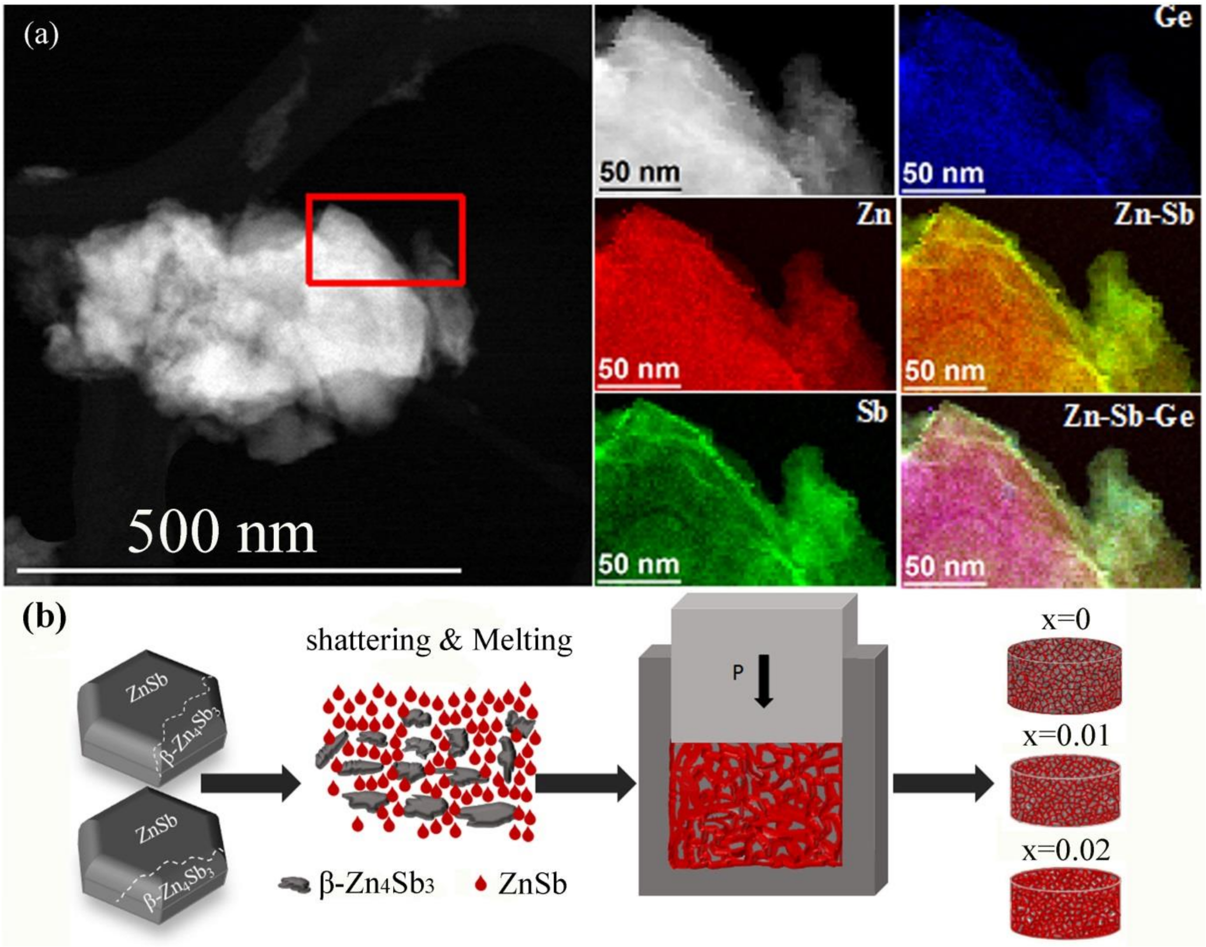

Figure 3. (a) EELS chemical composition maps obtained from the red squared area of the STEM micrograph of $Zn_{1.08}Ge_{0.01}Sb$ nanocomposite. Individual Zn L2,3-edges at 1020 eV

(red), Sb M4,5-edges at 528 eV (green), Ge L2,3-edges at 1217 eV (blue), as well as the composite Zn-Sb and Zn-Sb-Ge elemental maps. (b) Schematic reprsentation of the ZnSb-(β-Zn_4Sb_3@ZnSb) nanocomposite formation.

2.3. Thermoelectric properties

The temperature dependence of the electrical resistivity, Seebeck coefficient and power factor of $Zn_{1.1-x}Ge_xSb$ nanocomposites containing different Ge substitution levels is plotted in **Figure 4**. The electrical resistivity of $Zn_{1.1}Sb$ decreased with increasing temperature, from 71.80 μΩm to 52.97 μΩm in the temperature range from ambient to 655 K, indicating a non-degenerate semiconductor behavior. The measured room temperature resistivity was close to the value of ~ 65 μΩm reported by Xiong et *al.*,[14] but it was considerably lower than values of 200 μΩm and 250 μΩm reported by Pothin et *al.*[30] and Valset et *al.*[36] for pure ZnSb. The relatively wide range of resistivities reported may be ascribed to the distinct level of intrinsic defects and off-stoichiometries and to the different amount and distribution of the β-Zn_4Sb_3 and ZnSb phases within materials produced using different synthesis techniques. Resistivities measured in the present work were higher than those previously reported for β-Zn_4Sb_3 compounds, which exhibited degenerate transport properties. Our results suggested that the electrical resistivity of $Zn_{1.1-x}Ge_xSb$ nanocomposites was a combination of the resistivity of the ZnSb matrix and the β-Zn_4Sb_3 domains, which presence reduced electrical resistivity. Besides, the electrical resistivity significantly decreased when introducing small amounts of Ge.

$Zn_{1.1-x}Ge_xSb$ nanocomposites exhibited p-type conductivity in the entire Ge-substitution range. The Seebeck coefficient decreased with increasing Ge substitution level, following the same trend as the electrical resistivity. The measured decrease of resistivity and Seebeck coefficient with the introduction of Ge may be related to an increase of the charge carrier concentration indirectly associated with the different electronegativity between Ge (2.01) and Zn (1.65) or their slightly different atomic radiuses, Ge (125 pm) and Zn (135 pm), which may result in a larger density of acceptor defects or a lower density of electron donors such as interstitial Zn due to a small lattice contraction.[29] Power factors significantly increased for all Ge-substituted nanocomposites with respect to undoped $Zn_{1.1}Sb$ as a result of a high reduction in the electrical resistivity and a moderate decrease in the Seebeck coefficients. All Ge-substituted nanocomposites exhibited very similar power factor in the entire temperature range, while $Zn_{1.08}Ge_{0.02}Sb$ exhibited a slightly higher PF at high temperatures. The maximum value of power factor for un-substituted $Zn_{1.1}Sb$ samples was 0.89 $mWm^{-1}K^{-2}$ at 650 K, which increased for Ge-substituted $Zn_{1.1-x}Ge_xSb$ nanocomposite up to 1.6 $mWm^{-1}K^{-2}$ for $x = 0.01$ and 1.65 $mWm^{-1}K^{-2}$ for $x = 0.02$ at the same temperature.

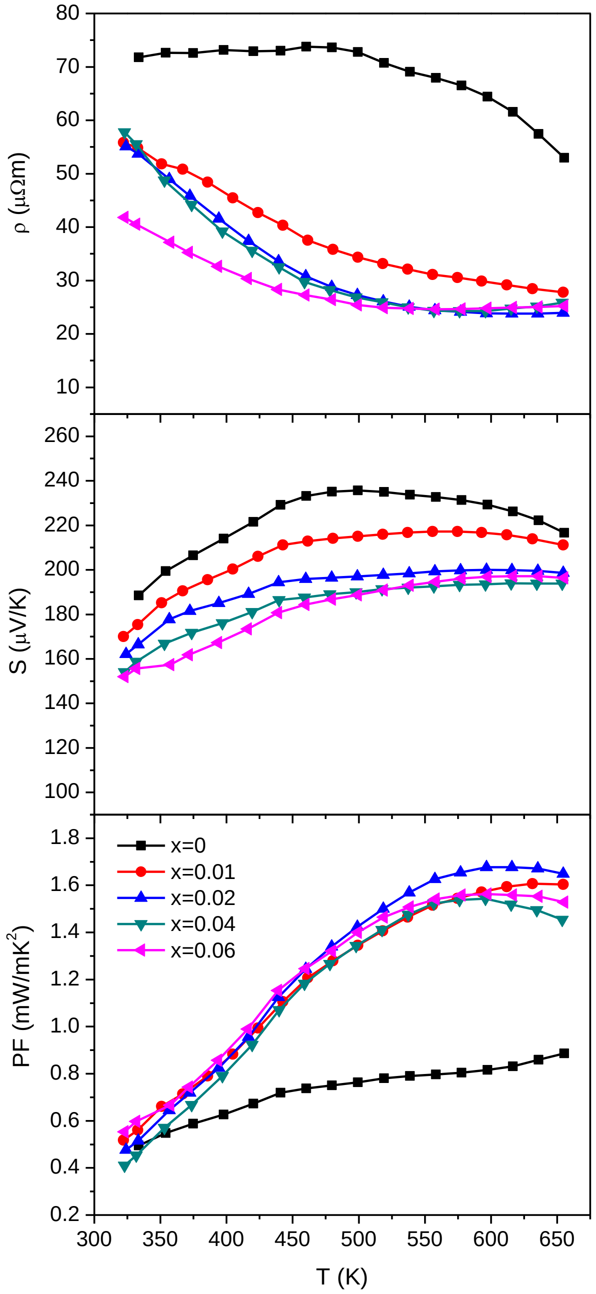

Figure 4. Temperature dependence of electrical resistivity (σ), Seebeck coefficients (S) and power factor (PF) for $Zn_{1.1-x}Ge_xSb$ nanocomposites.

Figure 5 shows the temperature dependence of the electronic thermal conductivity, κ_e, lattice thermal conductivity, κ_l, and total thermal conductivity, κ, of $Zn_{1.1-x}Ge_xSb$ nanocomposites. A relatively low thermal conductivity was measured for un-substituted $Zn_{1.1}Sb$ nanocomposites over the entire temperature range measured, reaching down to 0.74 $Wm^{-1}K^{-1}$ at 475 K. This value is much lower than those usually obtained for ZnSb. These results indicated that the presence of β-Zn_4Sb_3/ZnSb interfaces in $Zn_{1.1-x}Ge_xSb$ nanocomposites strongly reduced the thermal conductivity of this material. The thermal conductivities of $Zn_{1.1-x}Ge_xSb$ nanocomposites increased with the introduction of Ge. This experimental evidence was explained in part by the increase of the electronic component of the thermal conductivity, and in part by the decrease of the relative amount of β-Zn_4Sb_3, which is characterized by an ultralow thermal conductivity.[11]

The electronic thermal conductivity was evaluated using the Wiedemann-Franz equation, $\kappa_e = L\sigma T$, where T is absolute temperature, σ is electrical conductivity and L is Lorenz number that was estimated using the formula proposed by Snyder et *al.*[41] The lattice thermal conductivity was then calculated by subtracting the electronic thermal conductivity (κ_e) from the total thermal conductivity (κ_t). As can be seen in Figure 5a, κ_e significantly increased with Ge substitution level, especially in the high temperature range measured. For un-substituted nanocomposite, the value of κ_e was 0.079 $Wm^{-1}K^{-1}$ at room temperature and increased up to 0.20 $Wm^{-1}K^{-1}$. On the other hand, κ_e was 0.14 $Wm^{-1}K^{-1}$ at room temperature and increased to 0.44 $Wm^{-1}K^{-1}$ at 650 K for $Zn_{1.04}Ge_{0.06}Sb$. An almost opposite behavior was observed for κ_L, (Figure 5b), which showed a significant increase with increasing Ge-substitution level at low temperature ranges and an almost Ge-independent behavior at high temperatures. A lattice thermal conductivity of 0.86 $Wm^{-1}K^{-1}$ was obtained for un-substituted $Zn_{1.1}Sb$ nanocomposites at room temperature, which increased upon Ge doping and reached up to 1.59 $Wm^{-1}K^{-1}$ for $Zn_{1.04}Ge_{0.06}Sb$.

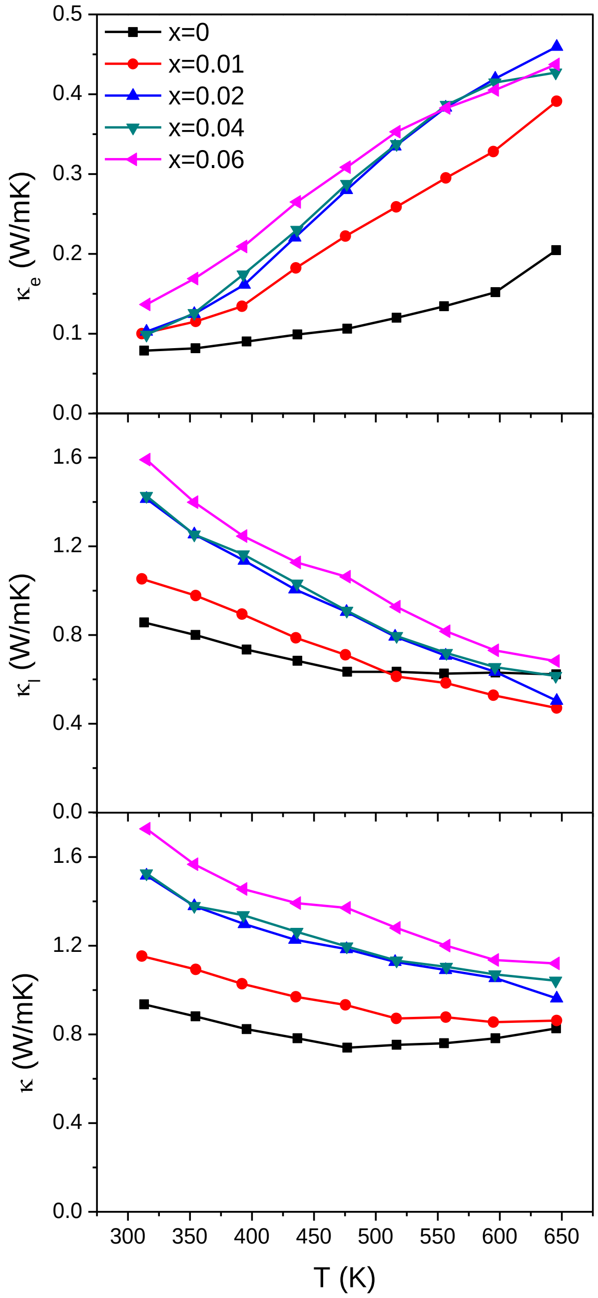

Figure 5. Electronic thermal conductivities (κ_e), lattice thermal conductivities (κ_l) and total thermal conductivities (κ) of $Zn_{1.1-x}Ge_xSb$ nanocomposite as a function of temperature.

Figure 6 shows the temperature dependence of *ZT* for $Zn_{1.1-x}Ge_xSb$ nanocomposites. Ge substitution induced an ample increase in *ZT* as a result of the substantial improvement in the power factor. An exceptional *ZT* value up to 1.2 was realized in $Zn_{1.09}Ge_{0.01}Sb$

nanocomposites at 650 K. This high *ZT* is almost twice the value obtained for un-substituted $Zn_{1.1}Sb$ nanocomposites. **Figure 7** shows the temperature dependence of *ZT* for our best performing $Zn_{1.09}Ge_{0.01}Sb$ nanocomposite in comparison to those reported in literatures for ZnSb compounds. It can be seen that $Zn_{1.09}Ge_{0.01}Sb$ has a higher ZT value than all those previously reported values for ZnSb. Especially, the maximum ZT value of 1.2, realized at a substitution level of $x = 0.01$, was more than twice the value reported for pure ZnSb.[30] To gain a deeper understanding of the TE performance of our nanocomposite, a comparison of thermal conductivity, Seebeck and electrical resistivity with previous papers is presented in **Figure S4**. The transport properties of $Zn_{1.08}Ge_{0.01}Sb$ nanocomposites was comparable to those of Ag-[12] and Cu-doped[36] samples. Our materials exhibited significantly lower thermal conductivities, very close to those reported for ZnSb/SiC nanocomposite,[41] suggesting the dominance of interface scattering. Furthermore, the obtained ZT values for $Zn_{1.09}Ge_{0.01}Sb$ were comparable to the best performing β-Zn_4Sb_3 TE materials.

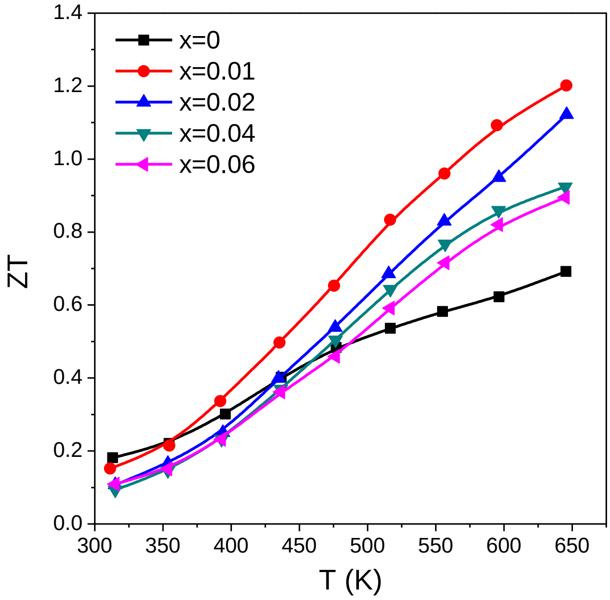

Figure 6. *ZT* values for $Zn_{1.1-x}Ge_xSb$ nanocomposite as a function of temperature.

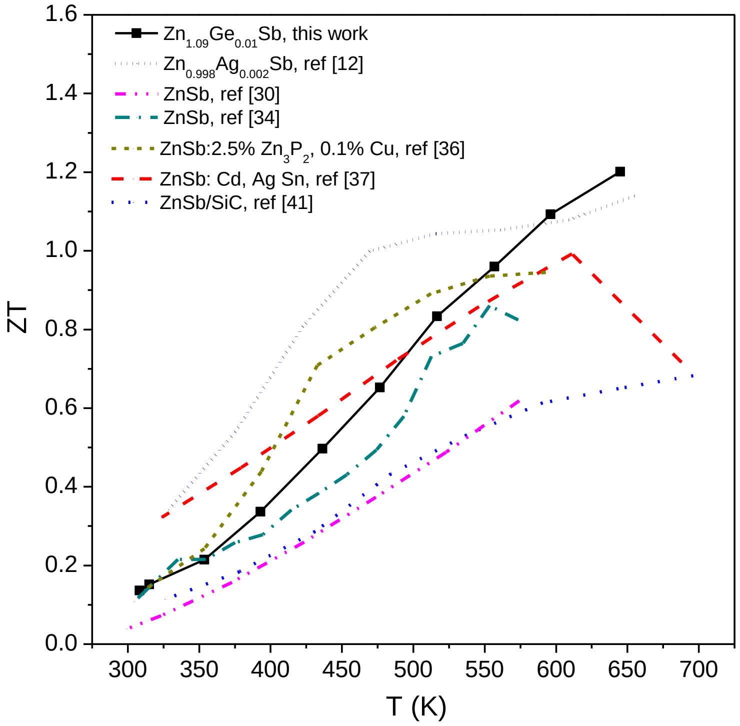

Figure 7. Temperature dependence of ZT for the best-performing sample studied here ($Zn_{1.08}Ge_{0.01}Sb$) and for best performing ZnSb materials previously reported.

Besides, our ZnSb/β-Zn_4Sb_3 nanocomposites exhibited superior stabilities than β-Zn_4Sb_3 TE materials. $Zn_{1.08}Ge_{0.01}Sb$ nanocomposites exhibited almost identical transport properties even after five cycles of measurements at a temperature up to 650 K (**Figure S5**). XRD patterns of $Zn_{1.08}Ge_{0.01}Sb$ nanocomposite (**Figure S6)** revealed very minor changes in the relative intensities of ZnSb and β-Zn_4Sb_3 peaks after 5 cycles of TE measurements. Quantitative Rietveld analyses indicated that the amount of β phase decreased from 35 % to 31 % with the TE measurements. Considering the high stability of the ZnSb phase, we believe that partially substituted ZnSb composites containing some fraction β-Zn_4Sb_3 nanoinclusions are promising TE materials deserving further investigation.

3. Conclusion

We developed ZnSb/β-Zn_4Sb_3 nanocomposites using a two-step approach. In a first step, $Zn_{1.1-x}Ge_xSb$ (x = 0, 0.01, 0.02, 0.04, 0.06) compounds were produced by a melting approach. In a second step, these compounds were ball-milled and hot-pressed. From this procedure, ZnSb/β-Zn_4Sb_3 nanocomposites consisting on small β-Zn_4Sb_3 grains surrounded by a ZnSb matrix were obtained. Ge doping led to a substantial decrease in the electrical resistivity concomitant to a moderate decrease in the Seebeck coefficient. As a result, the power factor significantly increased above 1.5 $mWm^{-1}K^{-2}$ at 550 K for all doped samples. The high density of ZnSb/β-Zn_4Sb_3 interfaces resulted in low thermal conductivities, down to 0.74 $Wm^{-1}K^{-1}$. Finally, a high and stable ZT value of 1.2 at 650 K was obtained for $Zn_{1.1-x}Ge_xSb$ at x = 0.01, which is among the highest values reported for ZnSb.

4. Experimental Section

Sample Preparation: Ge-doped ZnSb/ β-Zn_3Sb_4 nanocomposites with nominal compositions $Zn_{1.1-x}Ge_xSb$ (x = 0, 0.01, 0.02, 0.04, 0.06) were produced in a two-step process. First, proper amounts of the three elements were reacted at high temperature. High purity Zn (99.9%, Alfa-Aesar), Sb (99.5%, Alfa-Aesar) and Ge (99.999 %, Sigma-Aldrich) powders in the proper ratio, $Zn_{1.1-x}Ge_xSb$ (x = 0, 0.01, 0.02, 0.04, 0.06), were weighted inside an argon-filled glove box and loaded into a quartz ampoule. The ampoule was then repeatedly evacuated and re-filled with nitrogen for 3 times and finally sealed under vacuum, at about 10^{-4} Torr. The sealed ampoules were fixed vertically inside a furnace and heated to 527 °C at 100 °C/h and soaked at this temperature for 18 hours. The furnace was subsequently turned off and the samples were allowed to cool down to room temperature inside the furnace.

In a second step, ingots were ground in an agate mortar and placed into a zirconia jar to ball mill them for 20 h using tungsten carbide balls. A ball to powder mass ratio of 6:1 and a rotation speed of 400 rpm were used. The ball milled powders were loaded into a 8 mm diameter graphite die and hot pressed under argon atmosphere at 400 ºC for 5 min, under a pressure of 100 MPa. After these 5 min, the heater was turned off and the pressure was kept constant until temperature dropped to about 250 °C, at which point the pressure was released. The obtained pellets were then annealed at 380 ºC for 1 h under Ar atmosphere.

Characterization: X-ray diffraction (XRD) patterns were collected on a Bruker AXS D8 ADVANCE X-ray diffractometer (Cu–Kα radiation, λ = 0.154 06 Å). The GSAS-II package[42] was utilized for Rietveld refinements analysis. The maximum weighted factor (wR) was 4.43% for $Zn_{1.1}Sb$ and the minimum wR was 3.90% for $Zn_{1.1-x}Ge_xSb$ ($x = 0.06$) at room temperature. Transmission electron microscopy (TEM) studies were performed on a Zeiss Libra 120, operated at 120 kV. The morphology of the samples was examined using a Zeiss Auriga scanning electron microscope (SEM) at 5.0 kV. Energy dispersive X-ray spectroscopy (EDS), worked with Zeiss Auriga SEM device, was employed for elemental analysis. High-resolution TEM (HRTEM) and scanning TEM (STEM) studies were carried out using a field emission gun FEI Tecnai F20 microscope at 200 kV with a point-to-point resolution of 0.19 nm. High angle annular dark-field (HAADF) STEM was combined with electron energy loss spectroscopy (EELS) in the Tecnai microscope by using a GATAN QUANTUM filter. Seebeck coefficient and electrical resistivity were measured simultaneously in a LSR-3 LINSEIS system under helium atmosphere. Thermal conductivity was obtained as a product of thermal diffusivity (λ), heat capacity (C_p), and mass density of the specimen (ρ), ($k = \lambda \times \rho \times C_p$). Thermal diffusivity was measured using a XFA 600 Xenon Flash apparatus. The density values were obtained using the Archimedes' method. The Dulong-Petit approximation was used to obtain the specific heat (C_p).

Supporting Information

Supporting Information is available from the Wiley Online Library or from the author.

Conflict of Interest

The authors declare no conflict of interest.

Received: ((will be filled in by the editorial staff))
Revised: ((will be filled in by the editorial staff))
Published online: ((will be filled in by the editorial staff))

References

[1] C. S. Birkel, E. Mugnaioli, T. Gorelik, U. Kolb, M. Panthöfer, W. Tremel, *J. Am. Chem. Soc.* **2010**, *132*, 9881.

[2] G. S. Pomrehn, E. S. Toberer, G. J. Snyder, A. Van De Walle, *J. Am. Chem. Soc.* **2011**, *133*, 11255.

[3] J. Wang, K. Kovnir, *J. Am. Chem. Soc.* **2015**, *137*, 12474.

[4] A. He, V. Svitlyk, D. Chernyshov, Y. Mozharivskyj, *Dalton Trans.* **2015**, *44*, 20983.

[5] C.-W.T. Lo, B.R. Ortiz, E.S. Toberer, A. He, V. Svitlyk, D. Chernyshov, T. Kolodiazhnyi, S. Lidin, Y. Mozharivskyj, *Chem. Mater.* **2017**, *29*, 5249.

[6] M. Boström, S. Lidin, *J. Alloys Compd.* **2004**, *376*, 49.

[7] J. Lin, X. Li, G. Qiao, Z. Wang, J. S. Carrete, Y. Ren, L. Ma, Y. Fei, B. Yang, L. Lei, *J. Am. Chem. Soc.* **2014**, *136*, 1497.

[8] B. L. Pedersen, B. B. Iversen, *Appl. Phys. Lett.* **2008**, *92*, 161907.

[9] S. Schlecht, C. Erk, M. Yosef, *Inorg. Chem.* **2006**, *45*, 1693.

[10] Y. Mozharivskyj, Y. Janssen, J. L. Harringa, A. Kracher, A. O. Tsokol, G. J. Miller, *Chem. Mater.* **2006**, *18*, 822.

[11] L. Bjerg, B. B. Iversen, G. K. Madsen, *Phys. Rev. B* **2014**, *89*, 024304.

[12] L. Song, A. B. Blichfeld, J. Zhang, H. Kasai, B. B. Iversen, *J. Mater. Chem. A* **2018**, *6*, 4079.

[13] B. L. Pedersen, H. Yin, H. Birkedal, M. Nygren, B. B. Iversen, *Chem. Mater.* **2010**, *22*, 2375.

[14] D.-B. Xiong, N. L. Okamoto, H. Inui, *Scripta Mater.* **2013**, *69*, 397.

[15] T. Zou, X. Qin, Y. Zhang, X. Li, Z. Zeng, D. Li, J. Zhang, H. Xin, W. Xie, A. Weidenkaff, *Sci. Rep.* **2015**, *5*, 17803.

[16] F. Liu, X. Qin, H. Xin, *J. Phys. D: Appl. Phys.* **2007**, *40*, 7811.

[17] H.-J. Gau, J.-L. Yu, C.-C. Wu, Y.-K. Kuo, C.-H. Ho, *J. Alloys Compd.* **2009**, *480*, 73.

[18] B. L. Pedersen, H. Birkedal, E. Nishibori, A. Bentien, M. Sakata, M. Nygren, P. Frederiksen, B. B. Iversen, *Chem. Mater.* **2007**, *19*, 6304.

[19] S. Wang, H. Li, D. Qi, W. Xie, X. Tang, *Acta Mater.* **2011**, *59*, 4805.

[20] D. Li, H. Hng, J. Ma, X. Qin, *J. Mater. Res.* **2009**, *24*, 430.

[21] D. Li, X. Qin, *Intermetallics* **2011**, *19*, 1651.

[22] W. Li, L. Zhou, Y. Li, J. Jiang, G. Xu, *J. Alloys Compd.* **2009**, *486*, 335.

[23] D. T. Ngo, L. T. Hung, N. Van Nong, *ChemPhysChem* **2018**, *19*, 108.

[24] M. Liu, X. Qin, C. Liu, L. Pan, H. Xin, *Phys. Rev. B* **2010**, *81*, 245215.

[25] L. Pan, X. Qin, H. Xin, D. Li, J. Sun, J. Zhang, C. Song, R. Sun, *Intermetallics* **2010**, *18*, 1106.

[26] L. Zhou, W. Li, J. Jiang, T. Zhang, Y. Li, G. Xu, P. Cui, *J. Alloys Compd.* **2010**, *503*, 464.

[27] L. Pan, X. Qin, M. Liu, *Solid State Sci.* **2010**, *12*, 257.

[28] S. Wang, X. She, G. Zheng, F. Fu, H. Li, X. Tang, *J. Electron. Mater.* **2012**, *41*, 1091.

[29] S. Wang, X. Tan, G. Tan, X. She, W. Liu, H. Li, H. Liu, X. Tang, *J. Mater. Chem.* **2012**, *22*, 13977.

[30] R. Pothin, R. Ayral, A. Berche, D. Granier, F. Rouessac, P. Jund, *Chem. Eng. J.* **2016**, *299*, 126.

[31] A. Ostovari Moghaddam, A. Shokuhfar, A. Cabot, *J. Alloys Compd.* **2018**, *750*, 1.

[32] A. Ostovari Moghaddam, A. Shokuhfar, A. Cabot, A. Zolriasatein, *Powder Technol.* **2018**, *333*, 160.

[33] A. Ostovari Moghaddam, A. Shokuhfar, P. Guardia, Y. Zhang, A. Cabot, *J. Alloys Compd.* **2019**, *773*, 1064.

[34] C. Okamura, T. Ueda, K. Hasezaki, *Mater. Trans.* **2010**, *51*, 860.

[35] X. Song, K. Valset, J. Graff, A. Thøgersen, A. Gunnæs, S. Luxsacumar, O. Løvvik, G. Snyder, T. Finstad, *J. Electron. Mater.* **2015**, *44*, 2578.

[36] K. Valset, P. Böttger, J. Taftø, T. Finstad, *J. Appl. Phys.* **2012**, *111*, 023703.

[37] M. I. Fedorov, L. V. Prokof'eva, D. A. Pshenay-Severin, A. A. Shabaldin, P. P. Konstantinov, *J. Electron. Mater.* **2014**, *43*, 2314.

[38] P. Dharmaiah, H.-S. Kim, K.-H. Lee, S.-J. Hong, *Arch. Metall. Mater.* **2015**, *60*, 1417.

[39] F. Tseng, S. Li, C. Wu, Y. Pan, L. Li, *J. Mater. Sci.* **2016**, *51*, 5271.

[40] T. Akao,Y. Fujiwara, Y. Tarui, T. Onda, Z.-C. Chen, *J. Electron. Mater.* **2014**, *43*, 2047.

[41] H.-S. Kim, Z. M. Gibbs, Y. Tang, H. Wang, G. J. Snyder, *APL Mater.* **2015**, *3*, 041506.

[42] B. H. Toby, R. B. Von Dreele, *J. Appl. Crystallogr.* **2013**, *46*, 544.

The in-situ preparation of ZnSb/β-Zn_4Sb_3 nanocomposites through a novel route is investigated. Our approach leads to an outstanding high and stable ZT value of 1.2 for Ge-doped ZnSb/β-Zn_4Sb_3 nanocomposite, which is among the highest values reported for this material.

Keywords: Nanocomposite, Thermoelectric, β-Zn_4Sb_3, ZnSb, Ball milling

A. Ostovari Moghaddam*, A. Shokuhfar, Y. Zhang, T. Zhang, D. Cadavid, J. Arbiol, A. Cabot*

Ge-doped ZnSb/β-Zn_4Sb_3 nanocomposites with high thermoelectric performance

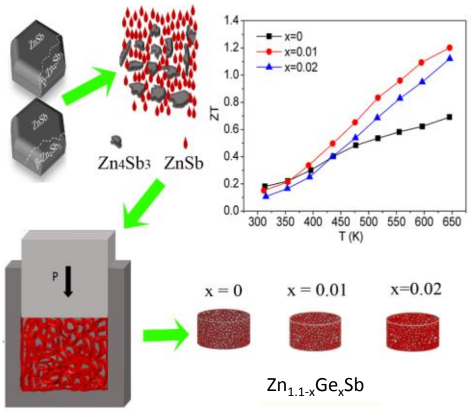

Supporting Information

Ge-doped ZnSb/β-Zn$_4$Sb$_3$ nanocomposites with high thermoelectric performance

Ahmad Ostovari Moghaddam, Ali Shokuhfar, Yu Zhang, Ting Zhang, Doris Cadavid, Jordi Arbiol, Andreu Cabot**

Dr. A. Ostovari Moghaddam, Prof. Ali Shokuhfar
Advanced Materials and Nanotechnology Research Laboratory, Faculty of Materials Science and Engineering, K. N. Toosi University of Technology, Tehran, Iran
E-mail: acabot@irec.cat, ostovary@aut.ac.ir

Y. Zhang, Prof. D. Cadavid, Prof. A. Cabot
Catalonia Institute for Energy Research – IREC, 08930 Sant Adrià de Besòs, Spain

T. Zhang, Prof. J. Arbiol
Catalan Institute of Nanoscience and Nanotechnology (ICN2), CSIC and BIST, Campus UAB, Bellaterra, 08193 Barcelona, Spain

Prof. D. Cadavid
Departamento de Física, Universidad Nacional de Colombia, 111321, Ciudad Universitaria, Bogotá, Colombia.

Prof. J. Arbiol and Prof. A. Cabot
ICREA, Pg. Lluis Companys 23, 08010 Barcelona, Spain

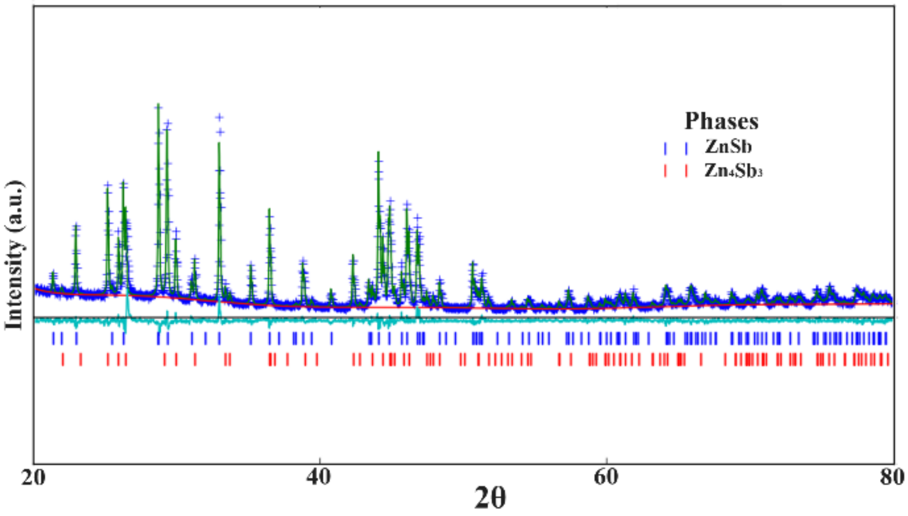

Figure S1. Rietveld refinement of the XRD pattern of the Zn$_{1.1}$Sb sample (wR = 4.43).

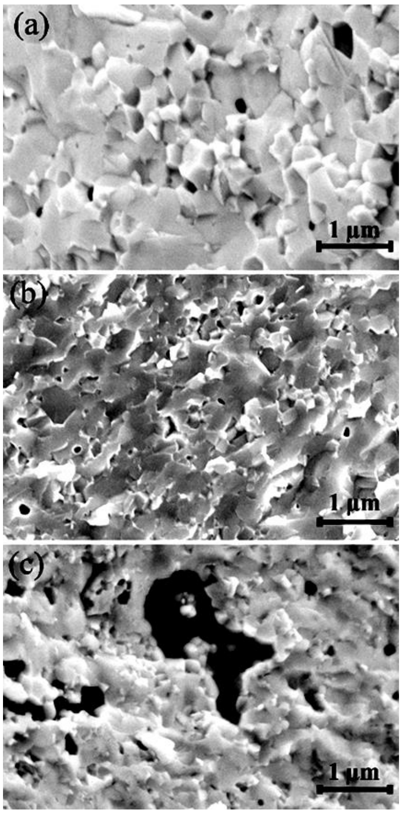

Figure S2. SEM micrographs of the fracture surface of $Zn_{1.1-x}Ge_xSb$ pellets for (a) *x* = 0, (b) *x* = 0.01 and (c) *x* = 0.06.

Table S1. Comparison between experimental and theoretical bulk plane spacing distances and angles between planes.

	R1	
Spot	Experimental (nm)	$Zn_{3.878}Sb_3$ (R3-CH) [11-20]
1	0.249	0.244 (4-40-2)
2	0.202 (41.99º vs Spot 1)	0.200 (41.94º) (5-50-2)
3	0.299 (96.10º vs Spot 1)	0.298 (96.77º) (1-10-4)
	R2	
Spot	Experimental (nm)	ZnSb (Pbca) [-121]
1	0.194	0.194 (311)
2	0.209 (50.92º vs Spot 1)	0.208 (50.20º) (222)
3	0.132 (83.59º vs Spot 1)	0.134 (82.26º) (135)

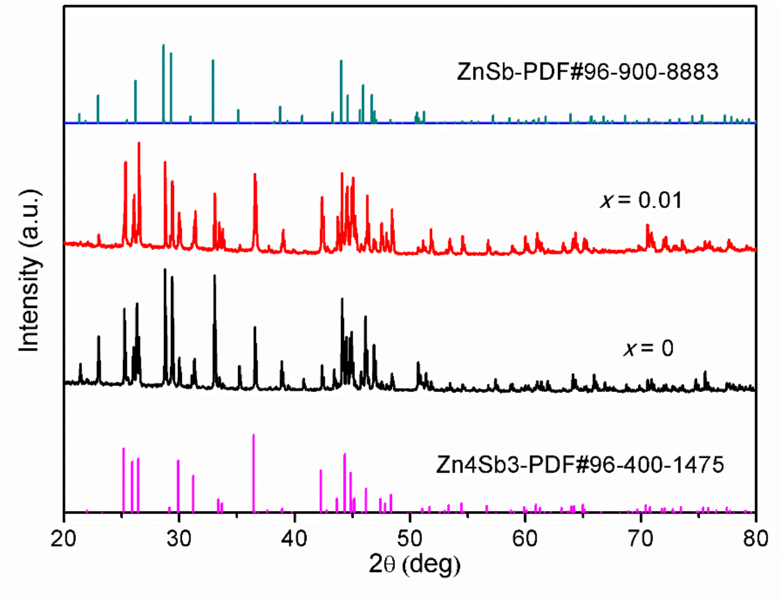

Figure S3. XRD patterns of $Zn_{1.1-x}Ge_xSb$ compounds (x=0, 0.01) after solid state reaction. Reference patterns for β-Zn_4Sb_3 (JCPDS 96-400-1475) and ZnSb (JCPDS 96-900-8883) are also plotted.

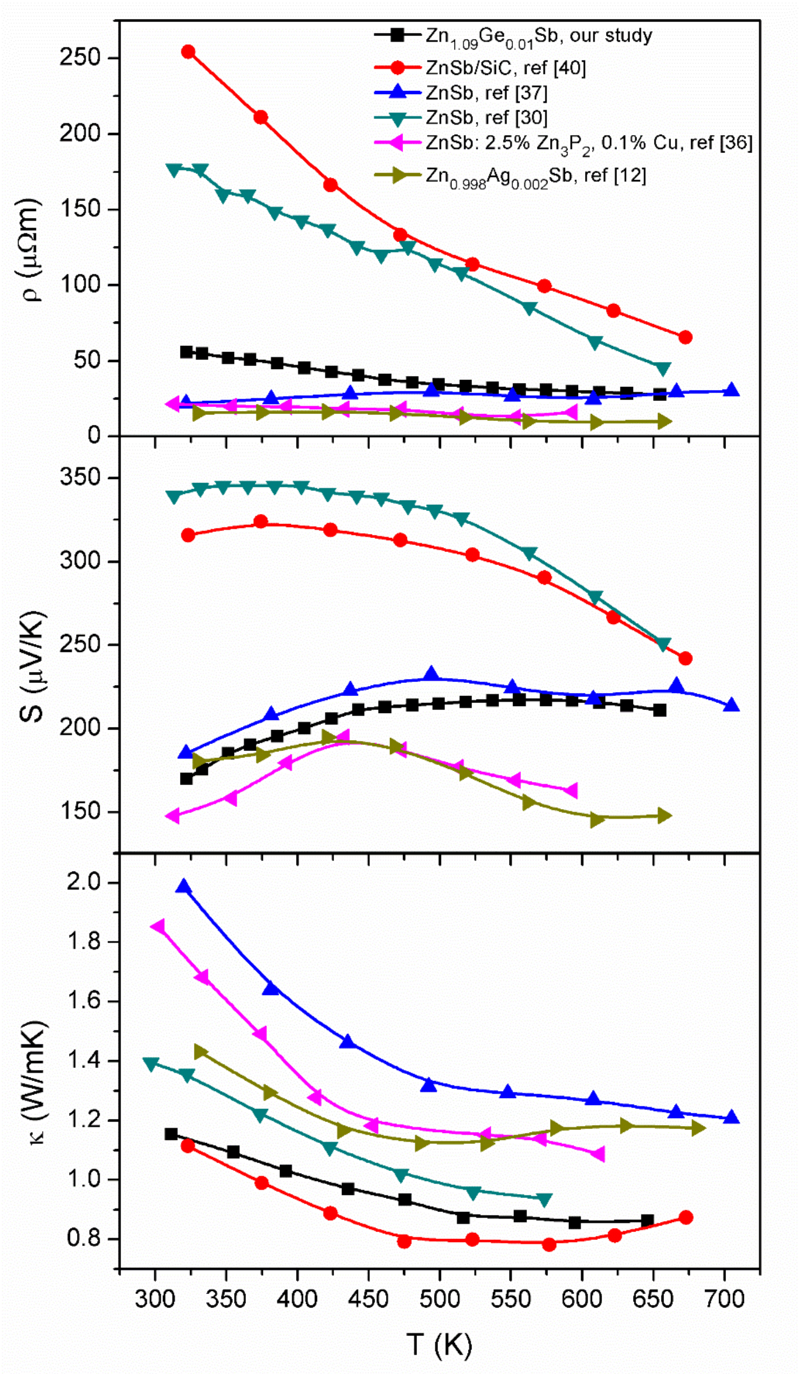

Figure S4. Temperature dependence of the TE properties for the best-performing sample ($Zn_{1.08}Ge_{0.01}Sb$) compared with literature data for ZnSb.

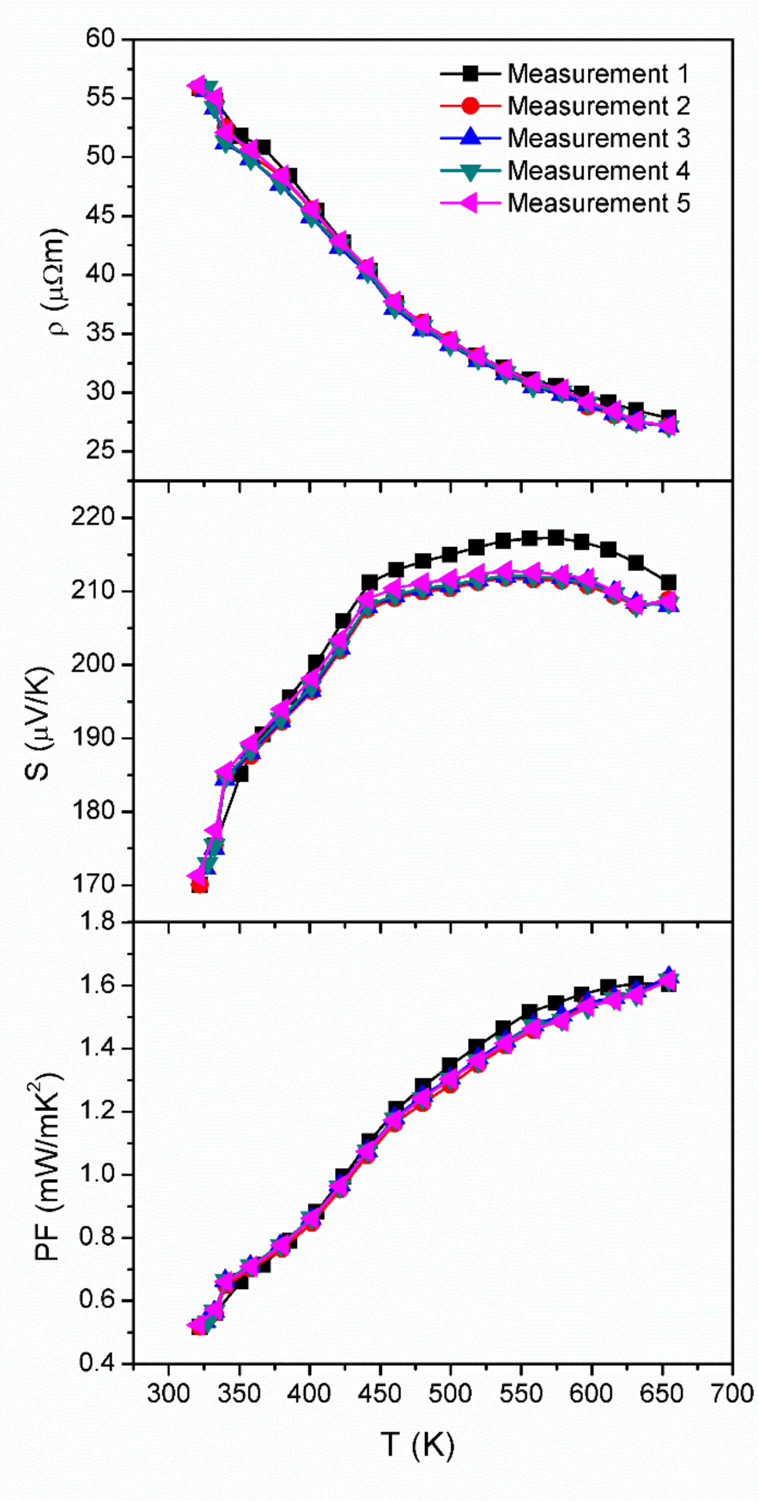

Figure S5. Repetitive measurement of electrical transport properties of $Zn_{1.1-x}Ge_xSb$ nanocomposite for x= 0.01.

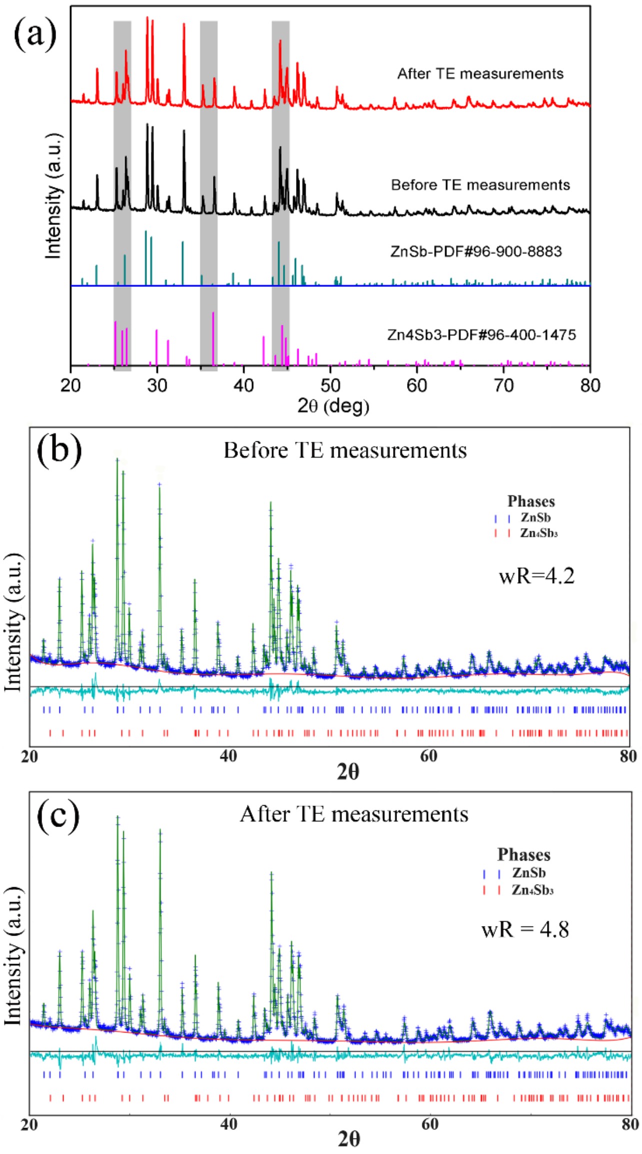

Figure S6. XRD patterns of $Zn_{1.09}Ge_{0.01}Sb$ nanocomposite (a), and Rietveld refinement performed on the XRD patterns before TE measurements (b) and after TE measurements (c).